Evaluation of high-resolution sea ice models on the basis of statistical and scaling properties of Artic sea ice drift and deformation.

Lucas Girard, Jérôme Weiss, Jean-Marc Molines, Bernard Barnier, S. Bouillon

Evaluation of high-resolution sea ice models on the basis of statistical and scaling properties of Arctic sea ice drift and deformation

L. Girard,[1] J. Weiss,[1] J. M. Molines,[2] B. Barnier,[2] and S. Bouillon[3]

[1] Sea ice drift and deformation from models are evaluated on the basis of statistical and scaling properties. These properties are derived from two observation data sets: the RADARSAT Geophysical Processor System (RGPS) and buoy trajectories from the International Arctic Buoy Program (IABP). Two simulations obtained with the Louvain-la-Neuve Ice Model (LIM) coupled to a high-resolution ocean model and a simulation obtained with the Los Alamos Sea Ice Model (CICE) were analyzed. Model ice drift compares well with observations in terms of large-scale velocity field and distributions of velocity fluctuations although a significant bias on the mean ice speed is noted. On the other hand, the statistical properties of ice deformation are not well simulated by the models: (1) The distributions of strain rates are incorrect: RGPS distributions of strain rates are power law tailed, i.e., exhibit "wild randomness," whereas models distributions remain in the Gaussian attraction basin, i.e., exhibit "mild randomness." (2) The models are unable to reproduce the spatial and temporal correlations of the deformation fields: In the observations, ice deformation follows spatial and temporal scaling laws that express the heterogeneity and the intermittency of deformation. These relations do not appear in simulated ice deformation. Mean deformation in models is almost scale independent. The statistical properties of ice deformation are a signature of the ice mechanical behavior. The present work therefore suggests that the mechanical framework currently used by models is inappropriate. A different modeling framework based on elastic interactions could improve the representation of the statistical and scaling properties of ice deformation.

Citation: Girard, L., J. Weiss, J. M. Molines, B. Barnier, and S. Bouillon (2009), Evaluation of high-resolution sea ice models on the basis of statistical and scaling properties of Arctic sea ice drift and deformation, *J. Geophys. Res.*, *114*, C08015, doi:10.1029/2008JC005182.

1. Introduction

[2] The sea ice cover is a dynamic body, moving under the action of winds and ocean currents. The deformation rates of sea ice, determined from the spatial gradients in the velocity field, are associated with internal stresses, which, when large enough, generate an ubiquitous network of fractures and leads. Fractures in the ice cover decrease the albedo and allow more shortwave absorption by the ocean, thereby shrinking the ice cover during summer, thus reducing its strength and possibly increasing the fracturing [*Moritz et al.*, 2002; *Zhang et al.*, 2000; *Rampal et al.*,

2009]. On the other hand, fracturing during winter enhances the thermodynamically driven production of new ice and modifies the heat and salinity budget in the Arctic [*Maykut*, 1982]. In all seasons, an increase of sea ice fracturing and fragmentation facilitates sea ice drift and its export toward lower latitudes [*Rampal et al.*, 2009]. Accurate modeling of the ice velocities and deformation rates is therefore essential in order to get a good representation of the open water fraction, the thickness distribution, and the global sea ice mass balance in climate models.

[3] Recent analysis of drifting buoy trajectories and fine scale sea ice kinematics produced by the RADARSAT Geophysical Processor System (RGPS) [*Kwok*, 1998b] expressed the heterogeneous and intermittent character of sea ice deformation by spatial and temporal scaling laws [*Marsan et al.*, 2004; *Rampal et al.*, 2008]. Investigation of internal sea ice stresses and RGPS-derived strain rates revealed the elasto-brittle behavior of the ice cover [*Weiss et al.*, 2007]: most of sea ice deformation is accommodated by active fractures and faults at various scales. This can explain the intermittency and spatial heterogeneity of sea ice deformation [*Weiss et al.*, 2009] but raises an important

---

[1]Laboratoire de Glaciologie et Géophysique de l'Environnement, CNRS/Université Joseph Fourier - Grenoble 1, St. Martin d'Hères, France.
[2]Laboratoire des Ecoulements Géophysiques et Industriels, CNRS/ Université Joseph Fourier - Grenoble 1, Grenoble, France.
[3]G. Lemaître Institute of Astronomy and Geophysics (ASTR), Université Catholique de Louvain, Louvain-la-Neuve, Belgium.

question: To what extent can current sea ice models simulate such a multiscale fracturing process?

[4] Indeed, current models stem from the work of *Hibler* [1979] who described the ice cover in terms of viscous-plastic (VP) mechanics and accordingly invoked the concept of a rate- and scale-independent failure envelope. This modeling framework is based on a fluid mechanics approach which seems at odd with a scenario where sea ice deformation is accommodated by multiscale fracturing processes.

[5] *Thomas* [1999] performed a comparison of model deformation fields and buoy-derived deformation estimates at large scale (400 to 600 km). He found modest correlation for vorticity and shear, but the correlations of divergence were insignificant. More recently, RGPS derived strain rates allowed a closer investigation of sea ice deformation on a wide range of spatial scales. *Lindsay et al.* [2003] and *Kwok et al.* [2008] used this new data set to examine model deformation rates from regional (~300 km) to small spatial scales (10 km). These two studies showed that even though models are capable of reproducing the large-scale drift patterns, the simulated deformation rates show rather poor correlation with RGPS observations, especially at small scales. Moreover, there is a high variability among models on these aspects.

[6] Although a high correlation between model and observation estimates of strain rates is desirable, it could be searched in vain. Indeed, sea ice velocity fluctuations have a stochastic component, implying that the spatial gradients of the velocity field also behave in a non deterministic manner. Using drifting buoy trajectories, Rampal et al. (Arctic Sea ice velocity field: General circulation and turbulent-like fluctuations, submitted to *Journal of Geophysical Research*, 2009, hereinafter referred to as Rampal et al., submitted manuscript, 2009) developed a methodology based on an analogy to fluid turbulence in order to determine the spatial and temporal averaging scales at which the velocity field can be partitioned into a mean component (i.e. the predictable part of velocity), and its respective fluctuations (i.e. the stochastic component). Considering the stability of the Lagrangian statistics, these authors established that the appropriate averaging scales to define the mean velocity field are 400 km spatially and 160 days temporally (in winter). The stochasticity of strain rates becomes dominant at scales below a few hundred km. With the grid size of models reaching ~10 km nowadays, it appears crucial to take this aspect into account when investigating the performance of models in terms of ice drift and deformation.

[7] These points have motivated an additional investigation of model ice drift and deformation using statistical comparisons with observations. In this paper, we examine probability distribution functions (PDF) of model strain rates at different scales and analyze the dependence of strain rates upon spatial and temporal scales. For this purpose, we use the methodologies developed by *Marsan et al.* [2004] and *Rampal et al.* [2008] to analyze buoy as well as RGPS data. This adds to the work of *Lindsay et al.* [2003] who underlined the necessity to evaluate the distribution functions of strain rates in models, in particular divergence, which influences most the ice production estimates.

[8] We have analyzed two simulations performed with the Louvain-La-Neuve Ice Model (LIM), coupled to a high-resolution global ocean model. A third simulation obtained with the Los Alamos sea ice model (CICE) was also examined. As this last simulation was obtained with a very different configuration, only a few features concerning ice deformation are presented. The fine grid size of these simulations (~12 km for LIM and ~9 km for CICE) allows the investigation of the scaling properties over a large-scale range and is of the same order of magnitude as the scale of RGPS observations (~10 km).

[9] This paper is organized as follows. The statistical properties of sea ice deformation on which our evaluation is based are summarized in section 2, along with the observation data sets they concern. Section 3 briefly describes the models. In section 4 model ice drift is evaluated, while model strain rates are considered in section 5. The results are discussed in section 6 and the conclusions are given in section 7.

2. Statistical and Scaling Properties of Sea Ice Deformation: Spatial Heterogeneity and Intermittency

[10] It is qualitatively known from the journey of Fridtjof Nansen on the Fram along the transpolar drift, at the end of the 19th century, that sea ice dynamics is characterized by tortuous drifting trajectories and intermittency, with a wide range of ice velocities and accelerations. As shown below, spatial heterogeneity and intermittency are the two main characteristics of sea ice deformation.

[11] The fine-scale sea ice kinematics produced by RGPS have allowed the investigation of sea ice motion and deformation over an unprecedented range of spatial scales, from 10 km to the scale of the Arctic Ocean as a whole (~1000 km). RGPS is based on a cross-correlation technique applied to consecutive SAR images [*Fily and Rothrock*, 1990], which allows tracking in a Lagrangian fashion of more than 40000 points over the Canadian side of the Arctic during an entire season. Data from 9 winters (1997–2008) are now available (http://www-radar.jpl.nasa.gov/rgps/), a database that has no counterpart in geophysics.

[12] The tracked points define the corners of cells which are initially squared (10×10 km^2). The velocities of the cell corners are computed over the period between two observations (sampled at irregular time intervals within the domain, but typically 3 days). The strain rate tensor components $\partial u/\partial x$, $\partial v/\partial x$, $\partial u/\partial y$, $\partial v/\partial y$ are computed from an approximation of the line integral around the boundary of each of the cells [*Kwok*, 1998b]. The 3 invariants of the strain rate tensor, respectively divergence, shear and vorticity, are defined as follows:

$$\dot{\epsilon}_{div} = \frac{\partial u}{\partial x} + \frac{\partial v}{\partial y} \tag{1}$$

$$\dot{\epsilon}_{shear} = \left[\left(\frac{\partial u}{\partial x} - \frac{\partial v}{\partial y} \right)^2 + \left(\frac{\partial u}{\partial y} + \frac{\partial v}{\partial x} \right)^2 \right]^{1/2} \tag{2}$$

$$\dot{\epsilon}_{vor} = \frac{\partial v}{\partial x} - \frac{\partial u}{\partial y} \tag{3}$$

The tracking errors (~100 m) give rise to error standard deviations of 0.5% day^{-1} in the divergence, shear, and vorticity [*Lindsay and Stern*, 2003].

[13] This data set revealed highly heterogeneous strain patterns with most of the deformations localized along so-called linear kinematics features (LKF) separating quasi-rigid plates [*Kwok*, 2001; *Moritz and Stern*, 2001]. However, this distinction is somewhat arbitrary as it relies on a chosen threshold, and is scale dependent. *Marsan et al.* [2004] performed a multifractal analysis of sea ice deformation from the RGPS database. For a 3-day interval centered around November, 5th, 1997, they computed the scaling of the moments $\langle \dot{\epsilon}_{tot}^q \rangle$, where the so-called total strain rate is defined as: $\dot{\epsilon}_{tot} = \sqrt{\dot{\epsilon}_{div}^2 + \dot{\epsilon}_{shear}^2}$. Note that this scalar quantity $\dot{\epsilon}_{tot}$ contains information about the intensity of the strain rate, whereas the information about the principal directions is lost. This procedure can be repeated over boxes of different sizes, from the size of the initial RGPS cell (10 km) to sizes close to the Arctic basin scale ($\sim$1000 km). A power law decrease of the average strain rate $\langle \dot{\epsilon}_{tot} \rangle$ with increasing scale L was observed, $\langle \dot{\epsilon}_{tot} \rangle \sim L^{-0.20}$. This is a signature of long-range spatial correlations present in the strain rate field, as a random spatial reshuffling of the strain rate values suppresses power law scaling [*Marsan et al.*, 2004]. A strong curvature of the experimental moment function $b(q)$, i.e. $\langle \dot{\epsilon}_{tot}^q \rangle \sim L^{-b(q)}$ where $b(q)$ is a nonlinear function of order q, was also reported, indicating multifractality of the strain rate. This multifractality expresses the scaling properties of sea ice deformation, and particularly the absence of characteristic scale between 10 and 1000 km, and show how the strain rate distribution evolves with the spatial scale considered. Consequently, determining threshold strain rate values to define LKFs is a scale-dependent procedure. In addition, the multifractality of the strain rate fields indicates that mean values carry limited information, due to the existence of extreme fluctuations, and actually depend on the spatial scale considered.

[14] The proportion (or density) of open water within the winter ice cover also exhibits a multifractal scaling behavior [*Weiss and Marsan*, 2004]. This similarity of the scaling properties of the strain rate field and the open water concentration is not a coincidence: it expresses the intimate link between fracturing and deformation at all scales and suggests that brittle deformation is essential in sea ice mechanics. Sea ice concentration is thus related to the deformation field, and has been shown to be one of the most important factors influencing the surface energy budget [*Sorteberg et al.*, 2007; *Lüpkes et al.*, 2008]. It appears therefore crucial to obtain a correct representation of the multifractal and scaling properties of sea ice deformation in climate models.

[15] The main limitation of RGPS is a time resolution of about 3 days that does not allow to explore the temporal scaling in details. For this purpose, the dispersion of buoys trajectories is an alternative. The idea to estimate sea ice deformation from buoys dispersion was first applied by *Thorndike* [1986], then used recently by *Rampal et al.* [2008] to analyze systematically the spatial and temporal scaling of sea ice deformation, from few hours to few months, and from few hundred meters to several hundred kilometers. A set of about 500 trajectories of drifting buoys were obtained from the International Arctic Buoy Program (IABP, http://iabp.apl.washington.edu/), deployed in the Arctic from 1979 until now. These buoys are fixed on the

ice and drift according to the ice motion. Positions are obtained from GPS receivers or Argos transmitters with a position uncertainty of the order of 100 m and 300 m, respectively [*Thorndike and Colony*, 1982; *Heil and Hibler*, 2002]. Like molecules in a gas or a turbulent fluid, nearby pieces of sea ice gradually move apart as the result of deformation [*Martin and Thorndike*, 1985]. In the case of fluid turbulence, it is customary to characterize this dispersion by the mean square change in separation r of pairs of fluid particles, $\langle \Delta r^2 \rangle$. In the case of the Arctic sea ice cover, it seems more appropriate to express this dispersion in terms of a deformation rate, using the standard deviation:

$$\dot{\epsilon}_{disp} = \left\langle \left(\frac{\Delta r}{\tau \times L} - \left\langle \frac{\Delta r}{\tau \times L} \right\rangle \right)^2 \right\rangle^{1/2} \qquad (4)$$

where L is the (initial) separation of the pair and the average is calculated over N pairs of buoys initially separated by $L \pm \delta L$ and over a time interval $\tau \pm \delta \tau$. A detailed explanation for the use of the standard deviation in the dispersion rate $\dot{\epsilon}_{disp}$, instead of the mean, is given by *Rampal et al.* [2008]. These authors applied such a methodology to the IABP data set in order to analyze the scaling properties of sea ice deformation.

[16] With this definition, $\dot{\epsilon}_{disp}$ only depends on deformation, i.e. not on solid rotation. However, the full strain rate tensor cannot be determined from pairs of trajectories, i.e. shear and divergence cannot be discriminated on this basis. *Rampal et al.* [2008] also demonstrated that $\dot{\epsilon}_{disp}$ is proportional to $\dot{\epsilon}_{tot}$, with a proportionality factor of about 4. Using appropriate binning of this data set, the authors obtained the temporal and spatial scalings of the strain rate $\dot{\epsilon}_{disp}$. The temporal scaling is characterized by:

$$\dot{\epsilon}_{disp} \sim \tau^{-\alpha(L)} \qquad (5)$$

where the power law exponent $\alpha(L)$ decreases with increasing spatial scale (initial separation), from $\alpha = 0.89$ for $L \approx 1$ km to $\alpha = 0.30$ for $L \approx 300$ km in winter (respectively 0.87 and 0.25 for summer). Relation (5) expresses the intermittency of the process. Indeed, a nonintermittent viscous flow would be characterized by $\alpha = 0$, whereas the boundary value $\alpha = 1$ would correspond to a deformation accommodated by an isolated event, corresponding to the activation of a single fracture or fault. Although the intermittent character, i.e. α, decreases toward large spatial scales as the result of averaging an increasing number of these events, sea ice deformation does not mimic viscous flow even at scales close to the Arctic basin scale.

[17] On the other hand, the following spatial scaling is obtained:

$$\dot{\epsilon}_{disp} \sim L^{-\beta(\tau)} \qquad (6)$$

where the exponent $\beta(\tau)$ decreases with increasing time-scale, from $\beta = 0.85$ for $\tau \approx 1$ hour to $\beta = 0.35$ for $\tau \approx 1$ month in winter (respectively 0.85 and 0.42 for summer). In this case, β expresses the degree of heterogeneity of sea ice deformation, bounded by $\beta = 2$ for a deformation localized along a single fracture, and by $\beta = 0$ for a homogeneous

deformation field (e.g., elastic or viscous). Sea ice deformation appears more homogeneous as one increases the timescale and therefore the number of deformation events, but a significant heterogeneity remains even at the scale of months, in agreement with the persistence of active structures over a season [*Coon et al.*, 2007]. The spatial scaling obtained from RGPS (see above) is in agreement with these results, although the dependence of β upon timescale was not explored with RGPS.

[18] Relations (5) and (6) therefore express the strongly intermittent and heterogeneous character of sea ice deformation, as well as the complex space-time coupling illustrated by the dependence of α on L and β on τ. They are essential features of sea ice deformation and dynamics upon which sea ice models performance can be evaluated.

3. Models Description

3.1. Common Framework for Ice Dynamics

[19] Most sea ice codes implemented in climate models are based on a continuum mechanics modeling framework following *Hibler* [1979], and share a common viscous-plastic (VP) rheology, assuming that sea ice has strength under convergence and shearing, but offers little or no resistance to divergence. In the original VP rheology, the momentum equation is solved implicitly over the whole ice pack. This rheology implies that for stress states inside the plastic yield curve the mechanical behavior is that of a viscous fluid, while the ice flows as a perfect plastic when the stress state reaches the yield curve.

[20] *Hunke and Dukowicz* [1997] developed a new method (Elastic-Viscous-Plastic, EVP) to solve the momentum equation explicitly, by introducing a nonphysical elastic term in the equation. This elastic term can be seen as a regularization of the singularity caused by small strain rates. Beyond this solving procedure, the mechanical framework remains very similar in VP and EVP solution techniques.

[21] The lack of physical basis of the VP/EVP framework has been underlined in the literature [*Nye*, 1973; *Weiss et al.*, 2007] but thanks to its numerical efficiency and suitability for coupling with ocean-atmosphere models, this framework has been widely used and is, nowadays, implemented in nearly all global coupled ocean-sea ice models.

3.2. LIM Simulations

[22] LIM was used as part of the global coupled ocean model DRAKKAR [*Barnier et al.*, 2006]. The configuration we used was developed for studying the evolution of the ocean variability under realistic atmospheric conditions over the last half century (1958–2004). It is based on ERA40 (until 2002), operational ECMWF analysis (after 2002), and satellite products, as detailed in Brodeau et al. (An ERA40 based atmospheric forcing for global ocean circulation models, submitted to *Ocean Modeling*, 2008). The effective spatial grid size of the configuration is about 12 km in the Arctic.

[23] LIM is a dynamic-thermodynamic sea ice model designed for climate studies [*Fichefet and Morales-Maqueda*, 1997]. The model dynamics are based on the two-category (consolidated ice and leads) approach of *Hibler* [1979], it employs the VP dynamics, but EVP dynamics was also recently implemented [*Bouillon et al.*, 2009]. The rheology

uses an elliptical yield curve and an ice strength parameter $P^* = 10000$ N m^{-2}.

[24] We present results from two simulations, using VP and EVP dynamics, with similar configurations, changing only the solution technique for ice dynamics. The simulations are referred to as LIMVP and LIMEVP. From these two simulations, 12 hourly fields of model ice drift have been analyzed from a three month winter period (January to March 1997).

[25] For the VP simulation, different values of the creep limit parameter have been tested but this did not affect significantly the statistical and scaling properties of ice deformation. The creep limit parameter corresponding to the results presented below is $\Delta_{\min} = 2 \times 10^{-8}$ s^{-1}. The LIMVP hindcasts compare well with observations in terms of ice extent and concentration [*Drakkar-Group*, 2007].

[26] The LIMEVP simulation was obtained as follows: (1) The model was initialized on the LIMVP simulation result on the 1 January 1995, (2) the model ran 1995 and 1996 with EVP dynamics, as 2 years of transition, and finally the 3-month period (January–March 1997) was extracted for this study. Not surprisingly, the EVP simulation shows very similar results in terms of ice extent, thickness and concentration, but because of the growing number of coupled model using this formulation, we included this second simulation in our analysis.

3.3. CICE Simulation

[27] CICE was developed by *Hunke and Lipscomb* [2001] for climate studies and differs from the original Hibler model in several aspects. It uses EVP dynamics, has five thickness categories and an ice thickness remapping scheme [*Lipscomb*, 2001] that transfers the ice between categories as it grows and melts. The grid size is 9 km. The ice strength is calculated through a ridging scheme initially presented by *Rothrock* [1975]. The ice was coupled to a simple ocean mixed layer that can absorb heat and grow ice in leads. More details about the configuration are given by *Maslowski and Lipscomb* [2003].

[28] While this simulation is different from the LIM simulations, we believe it is interesting to examine sea ice deformation produced by CICE as it includes several features that could improve the representation of ice dynamics: multiple ice categories and a parameterization of ice strength through a ridging scheme. Moreover, *Maslowski and Lipscomb* [2003] indicated that this simulation shows qualitatively more realistic ice strain fields, compared to other models, with stronger localization of deformation.

[29] The simulation years do not match the availability of RGPS observations. We used daily simulation data from January–March 1987, considered as representative of typical winter ice drift. As no direct comparison is possible, we restricted our analysis to a few salient features of sea ice deformation.

3.4. Common Projection and Study Area

[30] All model scalar and vector fields were projected onto a common Cartesian coordinate system centered on the North Pole (polar stereographic projection), with the vertical axis following the Greenwich meridian.

[31] Coastal regions are known to be of special character in terms of sea ice dynamics: boundary conditions and
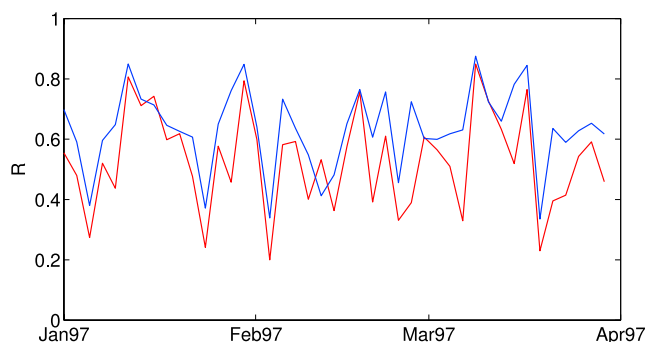
Figure 1. Time series of correlation coefficient R for model (LIMVP in red, LIMEVP in blue) against SSMI velocity field (2-day average, 83-km grid). R is calculated for vectors as complex numbers.

coastal geometry play an important role, the transition zone between fast ice and pack ice is characterized by particularly large sea ice strain rates, making the tracking of sea ice deformation in these regions difficult. Consequently, we limited our analysis to the central Arctic basin, north of Bering and Fram straits and 150 km away from the coastlines. In model simulations, the ice concentration over the considered region was always greater than 80% during the period analyzed.

4. Ice Drift

[32] This section compares ice drift from LIM simulations to observations at different scales. We first examine how the large-scale ice drift is represented in the simulations. We then consider probability distribution function (PDF) of ice velocity fluctuations.
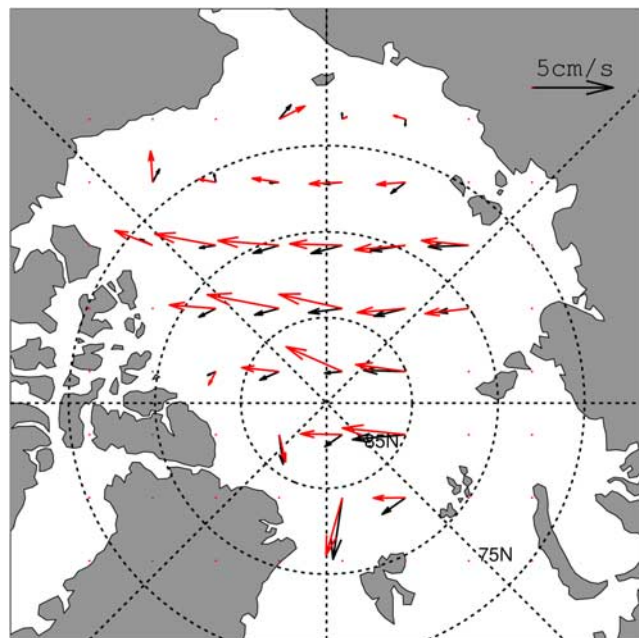

Figure 2. Mean ice velocity field for January–March 1997 at 400 km scale from the LIMVP simulation (red) and SSMI observations (black).

Table 1. Model and SSMI Ice Drift Statistics[a]

	83 km, 2 days			400 km, 3 months		
	SSMI	LIMVP	LIMEVP	SSMI	LIMVP	LIMEVP
Mean speed	4.3	7.8	6.9	1.3	3.3	3.0
Std (speed)	3.6	4.7	4.3	0.7	1.4	1.1
$\langle \Delta\theta \rangle$		47	32		24	23
R_{global}		0.57	0.70		0.83	0.82
N^{b}		650	650		28	28

[a]Mean speed (km/day) and standard deviation of the speed, mean angle difference between the model and SSMI drift vectors $\langle \Delta\theta \rangle$ (degrees), and global correlation coefficient between model and SSMI velocity drift vectors considered as complex numbers R_{global}.
[b]N is the number of points used for correlations.

4.1. Mean Velocity Field

[33] Before examining fluctuations and spatial gradients of ice drift, it is useful to check how well the mean velocity field is represented in the simulations.

[34] Observations from the Special Sensor Microwave Imager (SSMI) passive-microwave satellite sensor can be used to estimate two daily ice velocity from cross-correlation between two images. SSMI ice motion data set was provided by the JPL Remote Sensing Group [Kwok, 1998a]. The SSMI data are gridded and have better spatial coverage than the buoy data, which motivates their use to evaluate the model mean velocity field. The error standard deviation of velocity estimates is about 8 times larger than for the buoys: 0.058 m s^{-1} versus 0.007 m s^{-1} [Thorndike and Colony, 1980; Kwok, 1998a].

[35] Two comparisons are performed, the first one is at the scales of SSMI observations (two daily and 83 km), while the second one concerns the whole 3-month period at the spatial scale of 400 km. According to the work of Rampal et al. (submitted manuscript, 2009), the mean velocity at the scales of this second comparison corresponds to the predictable component of the velocity field.

[36] For the first comparison, model ice velocities are resampled to fit SSMI data spatially and temporally (linear interpolation to 83 km and two daily averaging), considering that SSMI estimates of ice velocity can be taken as point values at this scale. The correlation coefficient R is calculated for each pair of 2-day velocity fields, considering vectors as complex numbers (Figure 1). R shows a high variability, shifting between 0.8 and 0.2. The global correlation, calculated from all velocity values, is slightly higher for LIMEVP ($R_{global} = 0.57$) than LIMVP ($R_{global} = 70$).

[37] The second comparison is performed by binning the model and SSMI ice velocities on a 400 km grid to average it spatially, and temporally, to 3 months. At these scales, the correlation increases to $R = 0.83$ for LIMVP and $R = 0.82$ for LIMEVP (Figure 2).

[38] Both comparisons show a significant bias on the speed (Table 1). This bias is of the same order of magnitude in both simulations and does not vary significantly with scales, it also appears on Figure 2. The ice thickness appears well represented, with a 2.2 m mean thickness over the arctic with largest thicknesses along the Canadian Archipelago. Ice thickness is therefore not the cause of this speed bias. The velocity direction also shows a bias, which reduces at large scales. Tuning of parameters such as the wind drag coefficient could perhaps help reducing these biases, but it is not in the scope of this study.
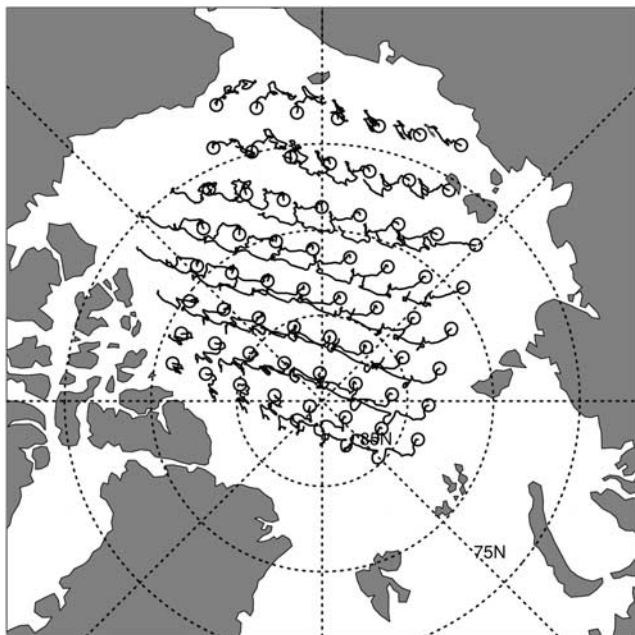
Figure 3. Example of reconstructed Lagrangian trajectories from Eulerian model outputs from January to March 1997. Circles indicate the initial grid points.

[39] The oscillation of the correlation values at small scale (83 km, 2 days) suggests that the model does not capture all spatial and temporal variability of the ice velocity field. At such scales, the motion of ice is dominated by stochastic fluctuations and is therefore not predictable in a deterministic sense. At 400 km and 3 months, a significant correlation is obtained, suggesting that the model captures well the mean ice circulation.

4.2. Velocity Fluctuations

[40] We consider the ice velocity as the sum of two components, an average ice drift and fluctuations. We calculate ice velocity fluctuations by subtracting the 400 km and 3 months average ice drift from ice velocity. Fluctuations of ice velocity result from short term wind-forcing, but also from the ice mechanical behavior, through the internal ice stress term of the equation of motion, which is calculated by the rheology.

[41] With a high temporal sampling of ice velocity (up to 3 h), drifting buoys provide the best observations to examine ice velocity fluctuations. Buoy measurements are of lagrangian type while model ice drift is eulerian.

[42] In order to make the comparison with buoy observations possible, model Eulerian ice velocity fields were used to reconstruct Lagrangian trajectories. Synthetic trajectories were initialized at each model grid point and obtained from a linear interpolation of the 12-hourly eulerian velocity fields, using the four nearest neighbors. We do not use an interpolation scheme of higher order to avoid an artificial smoothing of these trajectories. Examples of such reconstructed trajectories are shown on Figure 3. Model velocity fluctuations are then calculated by subtracting the average model ice drift interpolated along the trajectories from the ice velocity. Buoy velocity fluctuations are calculated similarly by subtraction of the average buoy drift from the velocities. The two standardized components (u' and v') of the model fluctuating velocity vector are represented through their PDFs (Figure 4), along with buoy measurements of velocity fluctuations performed between January and March from 1979 to 2001. All years of buoy measurements are considered to obtain a sufficient amount of data for the comparison, and the PDF obtained is assumed to be representative of a typical January–March period. We checked the validity of this assumption by plotting PDFs of buoy velocity fluctuations from specific years, and did
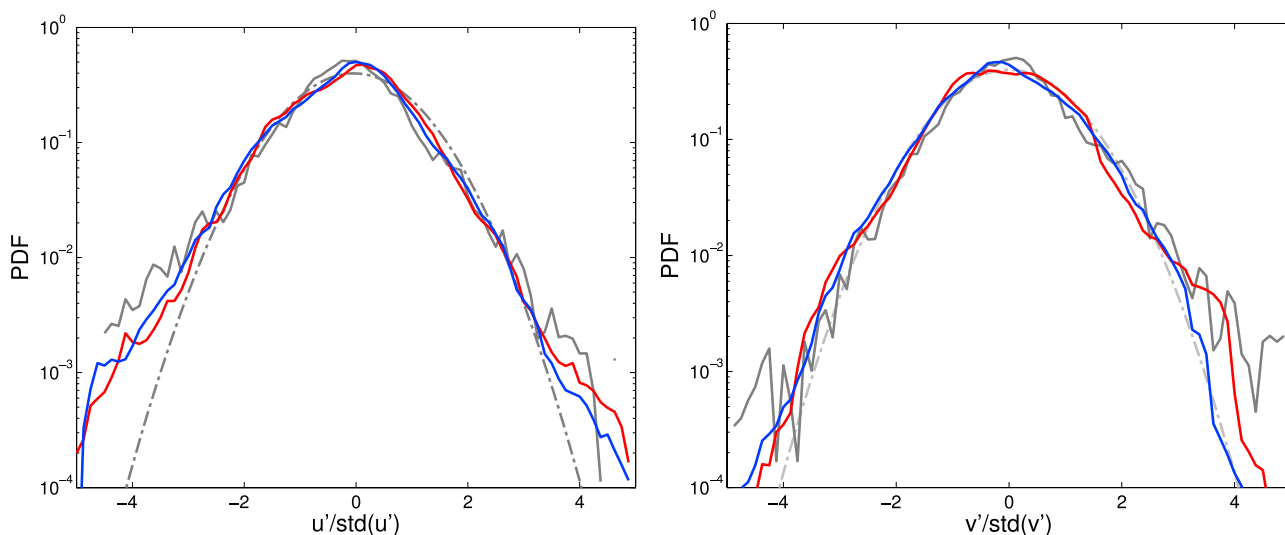

Figure 4. PDFs of the two components of velocity fluctuations of 12-hourly velocity (left, u' and right, v'), normalized by their standard deviation (buoys measurements: gray, model; LIMVP: red; LIMEVP: blue) and the corresponding Gaussian distribution (mean of 0 and standard deviation of 1, dashed line). The standard deviations are as follows: $\text{std}(u'_{buoys}) = 3.11$, $\text{std}(v'_{buoys}) = 3.28$, $\text{std}(u'_{LIMVP}) = 6.74$, $\text{std}(v'_{LIMVP}) = 6.05$, $\text{std}(u'_{LIMEVP}) = 6.13$, $\text{std}(v'_{LIMEVP}) = 5.53$.

not find any significant deviation from the data presented on Figure 4.

[43] Distributions presented on Figure 4 are standardized in order to focus the comparison on their shape. As for fluid turbulence, the shape of the PDF of velocity fluctuations, rather than its absolute standard deviation, is expected to characterize the underlying physical processes (see, e.g., *Frisch* [1995], for turbulence and Rampal et al. (submitted manuscript, 2009) for sea ice). The distributions of velocity fluctuations show similar shapes, suggesting that the model reproduces correctly the velocity fluctuations over the 3 months analyzed in this study, although the model slightly underestimates the tails of the PDF, i.e. the largest (relative) velocity values beyond 3 to 4 standard deviations. Both model and buoy distributions deviate from the Gaussian distribution in the tails.

[44] In order to investigate time correlations of velocity fluctuations, the mean temporal autocorrelation function of velocity fluctuations $C(\tau)$ was calculated for the reconstructed trajectories. $C(\tau)$ decreases with increasing time lag τ as particles loose the memory of their previous displacements and crosses zero in a finite time. A measure of how fast $C(\tau)$ decreases to zero is defined by the integral timescale Γ, obtained by integrating $C(\tau)$ up to the first zero crossing [e.g., *Zhang et al.*, 2001]. The integral timescale obtained is 2.9 days in both simulations, whereas the same calculation with drifting buoy trajectories leads to an integral timescale of 1.3 days (Rampal et al., submitted manuscript, 2009). In other words, the trajectory of a sea ice particle keeps memory of its previous displacements twice as long in the model as in the observations.

[45] If we assume that the correlation length is well represented in the model ice drift, considering the significant speed bias in the model (ice is drifting twice too fast), one would expect a smaller correlation timescale in the model. Since the correlation timescale we find is twice as long in the model as for buoys, it suggests a strong difference regarding the temporal evolution of model and observed ice drift. Although the velocity distribution seems correctly represented in the model, the temporal evolution of velocity might not be as well simulated. This suggests that processes leading to the decorrelation of ice velocity, such as the fracturing and ridging activity of the ice cover, are perhaps not correctly simulated.

5. Ice Deformation

[46] Sea ice deformation is examined in this section, first through a qualitative analysis of strain rate fields, then by comparing distributions of model and RGPS strain rates. Finally, we investigate the dependence of model strain rates upon spatial and temporal scales using the methodologies developed by *Marsan et al.* [2004] and *Rampal et al.* [2008] to analyze RGPS and buoy data.

5.1. Strain Rate Fields

[47] Model Lagrangian trajectories presented in the previous subsection are used to compute the strain rates following the same procedure as for RGPS (see section 2). We do this in order to ensure the best comparability of model and RGPS strain rates, the latter being calculated within a Lagrangian framework. A coarse graining procedure is applied to obtain model strain rates on a wide range of spatial scales, from the model grid size ($\sim$12 km) up to 1000 km. A temporal scale of 3 days is used to fit with the average sampling time interval of RGPS. The complete range of RGPS sampling intervals allowed for the analysis is 2 to 6 days.

[48] Figure 5 shows an example of LIM and RGPS strain rate fields at fine spatial scale, respectively 12 km and 10 km for the time period 16–18 January 1997. It makes sense to consider the model strain rate at this scale because the rheology introduces variability at the grid scale, although it is smoothed by stability operators. It is certainly not expected that LIM should be able to reproduce the details of ice deformation at such scales. Beyond resolution problems, the importance of the stochastic component of ice velocity at such small scales needs to be accounted for. This implies that even if the model physics was perfect, the strain rates could not be predicted in a deterministic sense. With all these considerations in mind, it is still trustworthy to analyze the general aspects of the model deformation fields from the example of Figure 5. The LIMVP strain rate fields appear very smooth and homogeneous, with large patches of divergence and shear. The large regions with convergence ($\dot{\epsilon}_{div} < 0$) are surprising, considering the near 100% ice concentration over the whole area. In winter, when sea ice is confined into the Arctic basin, a pattern with large patches of convergence is incompatible with the mechanical behavior of a fractured plate for which convergence is associated with the closure of freshly opened fractures and the formation of pressure ridges, i.e. is necessarily strongly localized along narrow faults. The LIMEVP simulation shows linear-like features that can span over several hundred km, but they are not structured as clearly as the so-called Linear Kinematic Features (LKFs) seen in RGPS observations.

[49] To further illustrate this differences, we considered the total amount of shear measured and simulated on this 3-day period. We calculated the fraction of ice surface area over which the highest values of shear were accommodated: At the scale of 10 km, in RGPS observations, 50% of all shear is accommodated by only 6% of the ice surface area, while in LIMVP and LIMEVP, it spans over respectively 23% and 18% of the surface area. The same calculation was done for shear rates at 100 km spatial scale. In this case, 50% of all RGPS derived shear is accommodated by 13% of the surface area, while 50% of all simulated shear spans over 22% of the surface area for LIMVP and 18% for LIMEVP. Similar values were obtained with other snapshots. These numbers express the fact that large shear rate values are extremely localized in RGPS observations, where a few percents of the surface hold most of the deformation at 10 km scale.

[50] An interesting point is that the localization of deformation in RGPS observations is scale dependent, i.e. decreases with increasing spatial scale. Opposingly, in the simulations, the spatial scale does not seem to affect the localization of deformation. Could this result be explained by the model resolution? or is there a physical discrepancy between the observed and simulated ice dynamics?

[51] The qualitative comparison presented in this subsection does not allow to differentiate these problems. The characteristics of strain rate distributions, presented in the
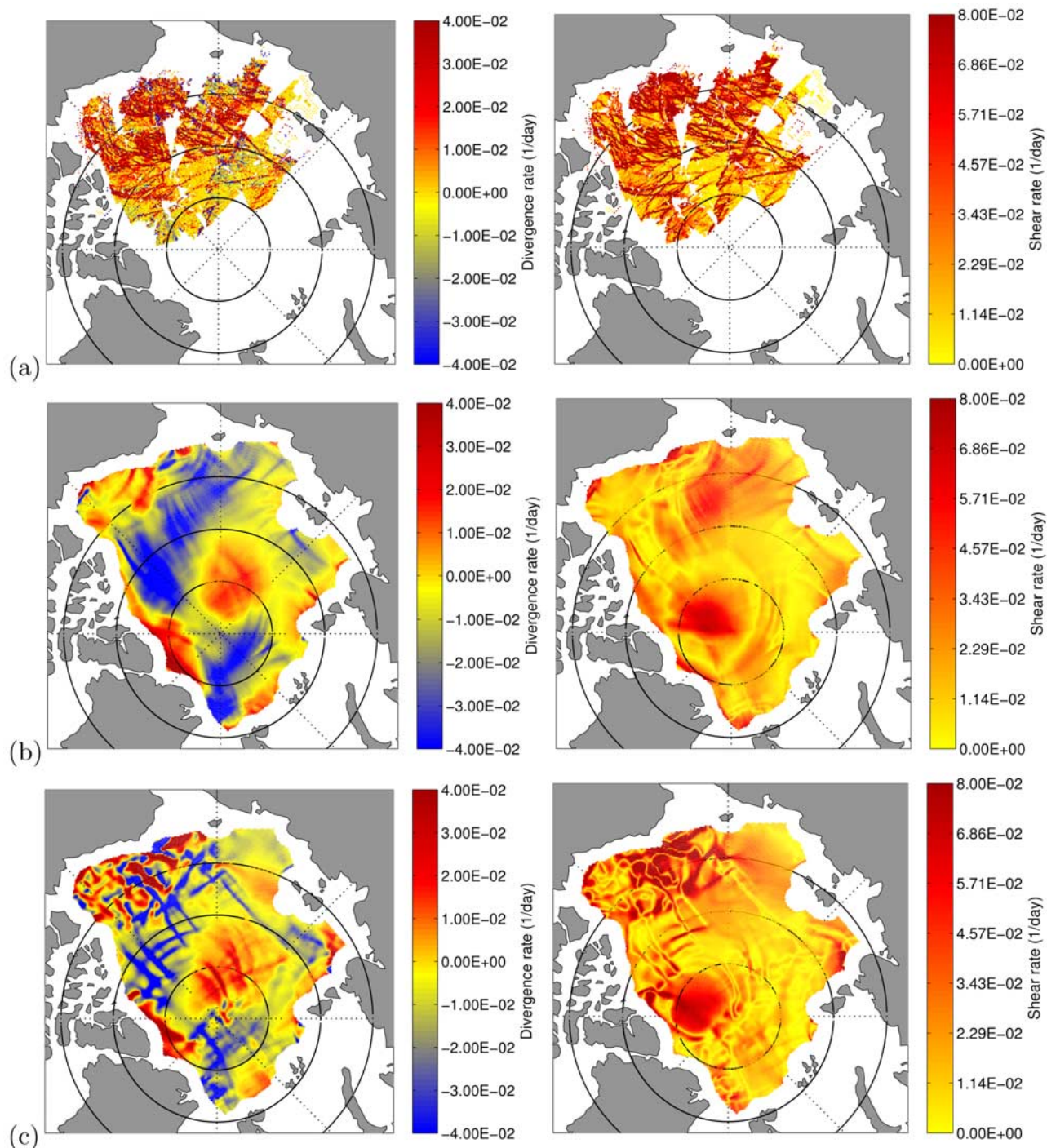
Figure 5. Divergence and shear rate fields (/day) from (a) RGPS observations, (b) LIMVP, and (c) LIMEVP for the period 16–18 January 1997.

following subsection, provide insights toward this direction. These results are complemented by a full analysis of the scale dependence of deformation over a broad range of spatial and temporal scales in section 5.3.

5.2. Strain Rate Distributions

[52] Figures 6, 7 and 8, compare the RGPS and LIM PDFs of respectively divergence, absolute value of divergence and shear. These PDFs are obtained from the whole period (January–March 1997) with RGPS and model strain rates at spatial scales of 10 km and 100 km and a temporal scale of 3 days. Table 2 gives the mean and standard deviations of these distributions and the ice speed statistics.

[53] The speed bias that appears in Table 2 is generally consistent with the results showed in section 4, the ice speed being faster in the model than in observations, but direct comparisons of the biases should be avoided since the observation data sets are very different in terms of accuracy and spatial coverage. In both simulations, the bias in the ice speed affects the spatial velocity gradients and thus the
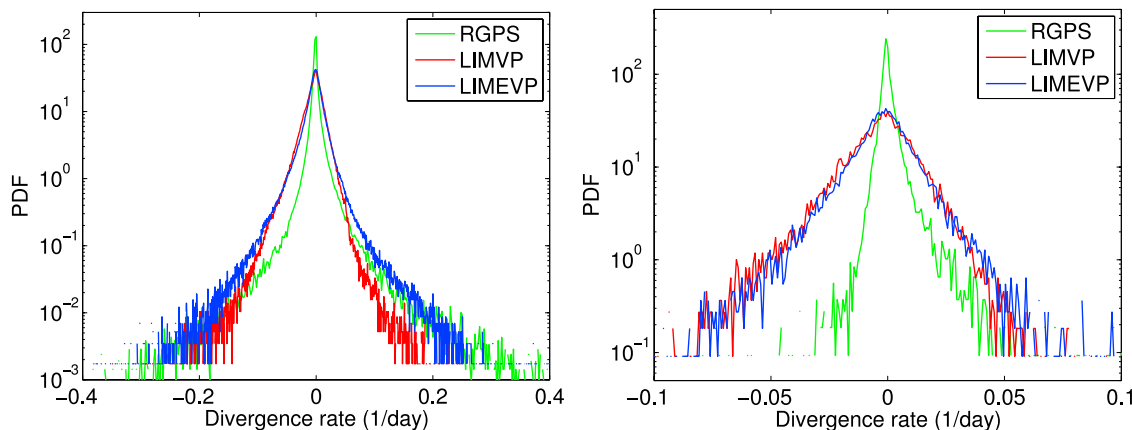
Figure 6. PDF of divergence rates for the period January–March 1997, from RGPS observations (green), LIMVP experiment (red) and LIMEVP (blue) at scales of (left) ~10 km and (right) ~100 km.

strain rates. This can presumably explain the difference between the mean shear rate in simulations and RGPS observations. The RGPS PDF of divergence rates shows an asymmetry toward positive values, which is notably marked at 100 km, while model PDFs are almost symmetrical with a slightly negative mean. At 10 km the standard deviations of model and RGPS strain rates differ by an order of magnitude but this discrepancy vanishes at 100 km. This does not imply that the model gets the right strain rate distribution at this scale. Instead, the shape of the distributions should be examined.

[54] Log-log scale plots (Figures 7 and 8) show clear differences between the model and RGPS strain rate distributions. The RGPS distributions of divergence and shear rates are fat tailed, following power law decays over two orders of magnitude ($p(\dot{\epsilon}) \sim \dot{\epsilon}^{-\eta}$), with slopes $\eta \leq 2.5$ at 10 km and in the range 2.6–3.3 at 100 km. This is consistent with the analysis of *Marsan et al.* [2004] for RGPS derived total deformation rates. Instead, the model distributions show exponential decays and do not have such a noticeable fat tail. Their slopes in a log-log scale (over the

last half order of magnitude) are at least 3.5 at 10 km and 5 at 100 km. At 100 km, model distributions are getting closer to the Gaussian distributions of same mean and standard deviation.

[55] The difference in the shape of the distributions is fundamental. Indeed, since they are not fat tailed, model PDFs are in the Gaussian attraction basin. This means that, by addition of random variable, they would converge toward a Gaussian distribution [e.g., *Sornette*, 2000]. In other words, they are associated with a "mild randomness".

[56] On the other hand, RGPS distributions follow Levy's laws of stability parameter $\mu = \eta - 1$ (where η is the slope of the power law). Such distributions are characterized by "wild randomness" and dominated by extreme values. When the distribution tail is shallow enough for $\mu \leq 2$, as for strain rate distributions at 10 km, the standard deviation is, analytically, infinity, while for $\mu \leq 1$ the mean is also undefined [*Sornette*, 2000]. In practice, it is always possible to compute an empirical mean and standard deviation for a given set of strain rates, but the shape of the RGPS distributions implies that the few largest values have sub-
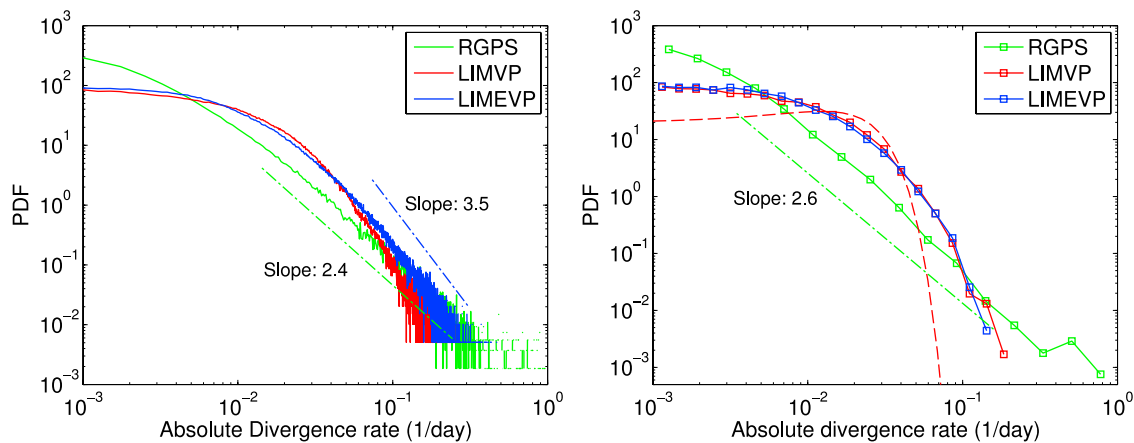

Figure 7. PDF of absolute value of divergence rates for the period January–March 1997, from RGPS observations (green), LIMVP experiment (red) and LIMEVP (blue), at scales of (left) ~10 km and (right) ~100 km. The green and blue dashed lines indicate, respectively, the slope of the RGPS and LIMEVP distributions. (right) The red dashed line is the Gaussian distribution of same mean and standard deviation as the LIMVP distribution.

Figure 8. PDF of shear rates for the period January–March 1997 from RGPS observations (green), LIMVP experiment (red), and LIMEVP (blue), at scales of (left) ~10 km and (right) ~100 km. The green and blue dashed lines indicate, respectively, the slope of the RGPS and LIMEVP distributions. (right) The red dashed line is the Gaussian distribution of same mean and standard deviation as the LIMVP distribution.
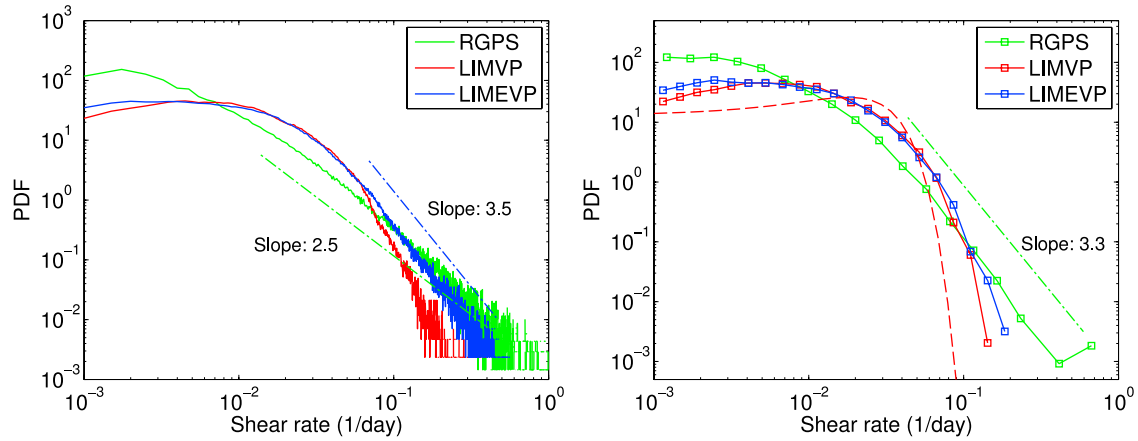
stantial influence on these empirical mean and standard deviation. This means that distributions of strain rates should not be compared only through their standard deviations and means, which are too volatile and dependent on the number of values considered. The comparison should instead consider the entire distributions. At 100 km, even if the standard deviation of RGPS and model strain rates are matching, the dissimilarity between the distributions actually increases: RGPS distributions are still power law tailed, whereas model distributions are getting closer to the Gaussian distribution.

[57] If the strain rates of the 10 km cells were independent scalar variables, identically distributed following Levy's law of parameter μ, the PDF of strain rates at any larger scale would also be a Levy's law of parameter μ. This is not exactly what is recovered here (μ tends to slightly increase with increasing scale), as strain rates are tensorial variables and strong spatial correlations exist. To fully analyze the evolution of the PDF with scale, a multifractal analysis is necessary. This is performed in the next subsection.

[58] As a point of comparison, Figure 9 shows the PDF of absolute divergence rates obtained with the CICE simulation. As no RGPS observations are available for the time period of the simulation, we restrict our analysis to a few comments regarding the shape of the distributions. The PDFs simulated by CICE are rather similar to the LIMEVP distributions, without significant improvement in the shape

of the PDFs. At 100 km the CICE PDF has an exponential decay and approaches the Gaussian distribution.

[59] This subsection has provided a first quantification of the strong discrepancy between simulated and observed strain rate fields qualitatively described in section 5.1 and Figure 5, as well as of the extreme localization of deformation within Arctic sea ice, a discrepancy that persists at scales much larger than the grid size. In the following subsection, we show that the existence of spatial and temporal correlations in the ice deformation field reinforces the discrepancy between models and observations.

5.3. Scaling Properties of Sea Ice Deformation

[60] As shown in section 2, sea ice deformation patterns are characterized by spatial as well as temporal scaling laws which are the signature of long-range correlations and space-time coupling.

[61] Three daily total deformation rates from January–March 1997 were binned with respect to their spatial scale (from 10 to ~1000 km). The mean deformation value of each bin and associated mean scale are represented on Figure 10, expressing the spatial scale dependence of total deformation rates, for RGPS observations and LIM simulations. At all spatial scales and a timescale of 3 days, a bias persists between the mean deformation of models and RGPS observations. This bias is consistent with the bias in the ice speed magnitude (the ice moves too fast in the

Table 2. Mean and Standard Deviations of Divergence and Shear Rate (1/day) at 10- and 100-km Scales, and Ice Speed Statistics (km/day)

		10 km, 3 days			100 km, 3 days		
		RGPS	LIMVP	LIMEVP	RGPS	LIMVP	LIMEVP
$\dot{\epsilon}_{div}$	mean	1.2×10^{-5}	-3.5×10^{-3}	-1.9×10^{-3}	1.2×10^{-3}	-3.1×10^{-3}	-1.7×10^{-3}
	std	0.17	0.019	0.22	0.016	0.017	0.017
$\dot{\epsilon}_{shear}$	mean	0.015	0.019	0.021	0.010	0.018	0.018
	std	0.23	0.17	0.025	0.020	0.015	0.017
Ice speed	mean	3.6	8.0	7.3	2.5	3.4	3.2
	std	3.0	5.0	4.4	2.6	1.5	1.2
N[a]		10^6	0.8×10^6	0.8×10^6	1.3×10^4	1.3×10^4	1.3×10^4

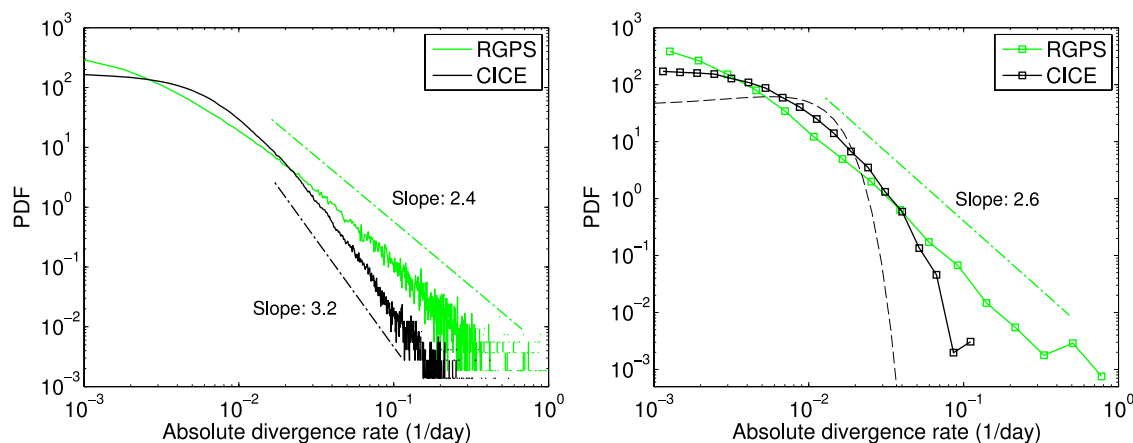[a]N is the number of observations or model values.

Figure 9. PDF of absolute value of divergence rates from the CICE simualtion (period January–March 1987) and from RGPS observations (period January–March 1997), at scales of (left) ~10 km and (right) ~100 km. (right) The black dashed line is the Gaussian distribution of the same mean and standard deviation as the CICE distribution.

model). However, this bias is not an essential criterion to test the accuracy of the simulations, as sea ice mean strain rates strongly depend, by nature, on the spatial and temporal scales considered, whereas modeled mean strain rates essentially do not. Consequently, one can find temporal and spatial scales at which simulations fit the observations, but this neither validates nor invalidates the model.

[62] Instead, we focus our analysis on the scale dependence of strain rates (i.e. the slope), which characterizes the heterogeneity of the deformation field. The scaling $\langle \dot{\epsilon}_{tot} \rangle \sim L^{-b}$ is observed over two orders of magnitude for RGPS observations. A least squares fit to the mean values (dashed line), gives an exponent $b = 0.18$ with a squared correlation 0.99. This is consistent with the results of *Marsan et al.* [2004] who obtained a similar scaling with an exponent $b = 0.2$ for RGPS observations of fall 1997.

[63] In the simulations, the power law scaling is not recovered. At small scales, the mean deformation simulated in LIMVP is nearly independent of L, then decreases for scales larger than ~200 km. This decrease could be explained by a finite-size effect: due to the confinement of the Arctic basin, a box of the order of the basin scale is not free to deform significantly. We note that for the scaling analysis of RGPS strain rate, this finite-size effect, which necessarily exists, is masked by the power law scaling. The scale dependence of LIMEVP mean deformation is slightly more pronounced than for LIMVP, but clearly not a power law.

[64] The difference between model and observations appears even more distinctly when considering the scale dependence of the moments $\langle \dot{\epsilon}_{tot}^{q} \rangle^{1/q}$ of order $q = 2$ and 3 (Figure 11). Moments of higher order give more weight to the large strain rate values. RGPS moments follow power laws with exponents depending on the moment order q, while LIM moments do not vary significantly with the moment order, neither with the spatial scale. For RGPS observations, the dependence of the exponent with q expresses the multifractal character of the strain rate field, in agreement with previous work [*Marsan et al.*, 2004], the fingerprint of the multifractal heterogeneity. This heterogeneity is absent for simulations.

[65] The results reported on Figures 10 and 11 show that the spatial correlations of deformation patterns are not correctly reproduced in LIM. The scale dependence of strain rates simulated by CICE was also examined (not shown here) through a similar procedure and did not match the power law decay either.

[66] As mentioned in section 2, RGPS is not suited to explore in details the temporal scaling as well as the space-time coupling of sea ice deformation, which was revealed by the analysis of the dispersion of buoys trajectories [*Rampal et al.*, 2008]. To evaluate the model performance on this basis, we used the reconstructed Lagrangian trajectories (see section 4.2) and followed the procedure presented in section 2 to estimate the strain rate proxy $\dot{\epsilon}_{disp}$ from dispersion rates. This was done for a wide spatiotemporal scale range, with initial separation L varying from ~10 km to ~500 km and time interval τ varying from 12 h
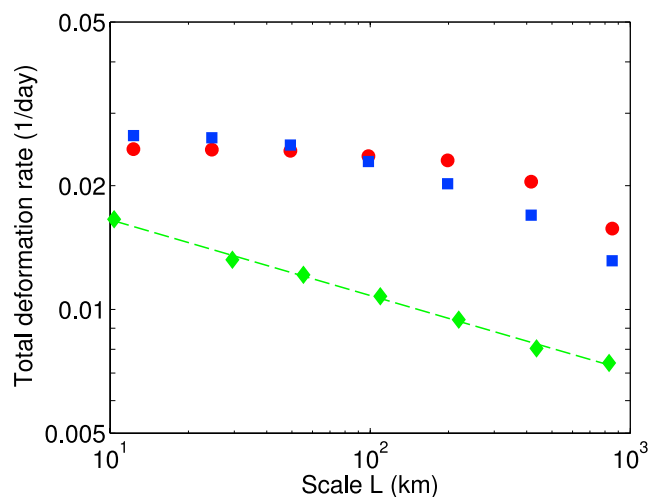

Figure 10. Mean total deformation rate $\langle \dot{\epsilon}_{tot} \rangle$ as a function of spatial scale L, obtained with RGPS observations (green diamonds), LIMVP (red circles), and LIMEVP (blue squares) simulations. The dashed line is the least squares fit for RGPS data $\langle \dot{\epsilon}_{tot} \rangle \sim L^{-0.18}$.
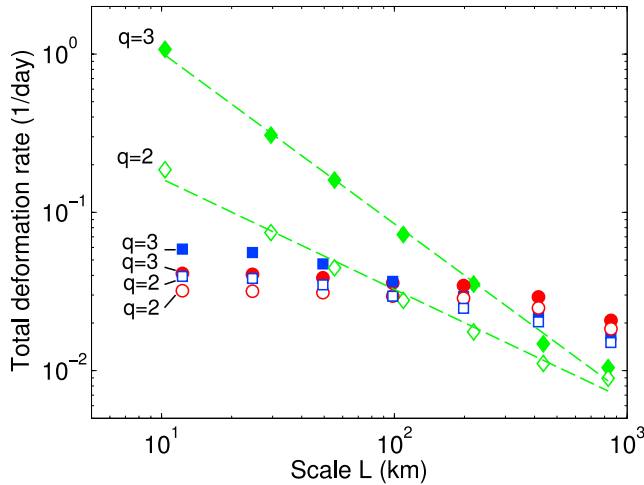
Figure 11. Moments of the total deformation rate $\langle \dot{\epsilon}_{tot}^{q} \rangle^{1/q}$ as a function of spatial scale L, for $q = 2$ and 3, for RGPS (green diamonds), LIMVP (red circles) and LIMEVP (blue squares). The dashed lines are least square fits for RGPS moments.

to 45 days. Model dispersion rates were then compared to dispersion rates obtained from IABP buoys trajectories during the January–March period, covering 23 years from 1979 to 2001.

[67] The differences between observed and modeled dispersion rates $\dot{\epsilon}_{disp}$ are striking (Figure 12): in both simulations, $\dot{\epsilon}_{disp}$ is nearly independent of the temporal and spatial scales considered, whereas it shows a strong decrease with scales when calculated from observations. Once again, Figure 12 shows that, to evaluate the perfor-

mance of a model, a comparison of mean strain rates performed at specific arbitrary scales is meaningless. Although simulations can match observations at some scales, the entire scale dependence should be checked.

[68] This discrepancy between models and observations confirms that (1) the models are unable to reproduce the spatial correlations of the deformation field and (2) that they do not reproduce the temporal correlations either.

[69] To illustrate the difference between simulations and observations, we calculated the ratio of the strain rate proxy at two different time intervals and spatial scales:

$$\frac{\dot{\epsilon}_{disp}[10 \text{ km}, 1 \text{ day}]}{\dot{\epsilon}_{disp}[300 \text{ km}, 50 \text{ days}]} \tag{7}$$

This ratio is ~ 2 in simulations, essentially as the result of finite size effect (see above), whereas it is more than one order of magnitude higher (~ 60) for buoy data.

[70] Moreover, the deformation rates estimated by both models agree with the observations at large spatial scales (100–300 km), suggesting that all the variability regarding sea ice deformation below such scales is missing in both models, regardless of their high resolution (~ 10 km grid size). This is consistent with the conclusions of *Taylor et al.* [2006] who suggested that the adoption of isotropic, continuum rheology at sub-100 km resolutions is not useful for a more detailed prediction of ice dynamics.

[71] Dispersion rates calculated with the CICE simulation were also examined and exhibit almost no temporal and spatial scale dependence compared to buoy dispersion rates.

[72] The dependence of $\dot{\epsilon}_{disp}$ upon time and spatial scales is an expression of the intermittency and heterogeneity of sea ice deformation, fully characterized by the scaling laws (5) and (6) (see section 2). These scaling laws are not
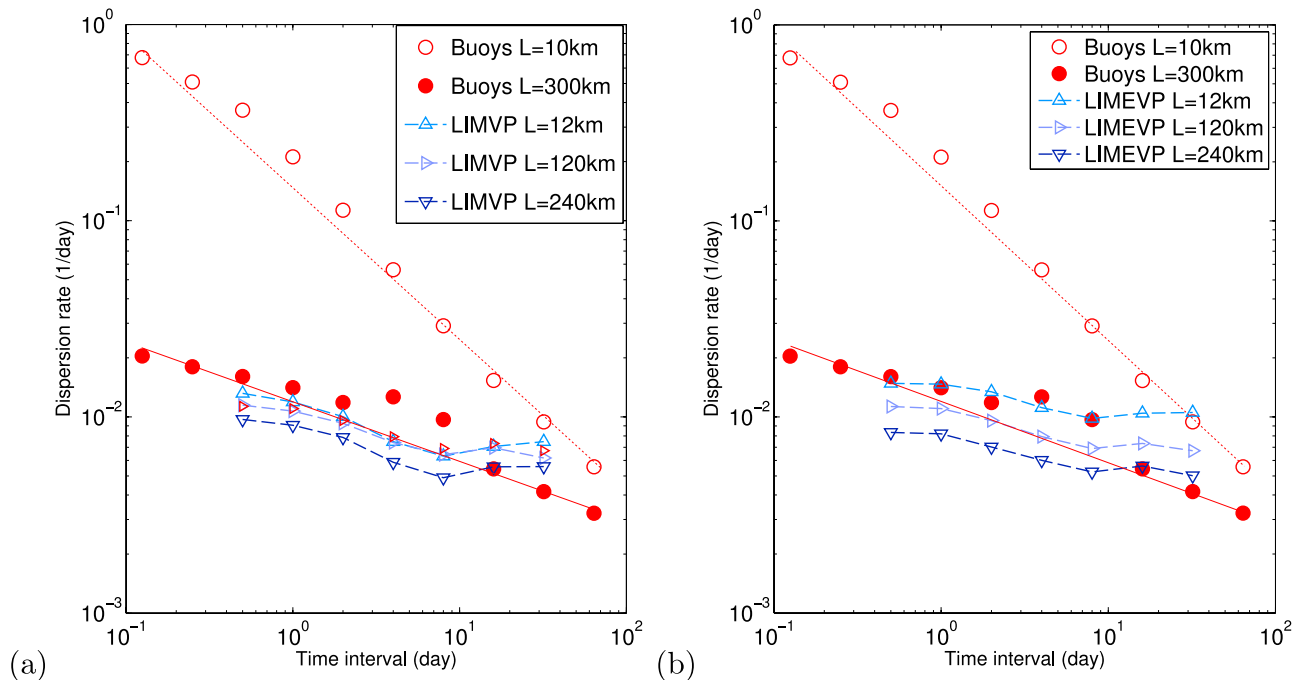

Figure 12. Spatial and temporal scale dependence of the dispersion rate $\dot{\epsilon}_{disp}$ for buoys data: (a) LIMVP and (b) LIMEVP. The dash lines are power law fits to buoys dispersion rates.

recovered in the models: The strain rate proxy $\dot{\epsilon}_{disp}$ is essentially independent of timescale as well as spatial scale, i.e. $\alpha \simeq \beta \simeq 0$. In other words, modeled sea ice behaves as a viscous fluid [*Rampal et al.*, 2008], with little spatial heterogeneity and no intermittency of the deformation.

6. Discussion

[73] This section discusses the causes of the discrepancy between model and observations. The influence of forcing and resolution problems against a real issue with the model physics is examined.

6.1. Insights From the Statistical Analysis of Ice Deformation

[74] The simulated mean ice drift field shows significant correlations with observations at large scales (400 km, 3 months) even though a large bias on the mean speed is noted and taken into account throughout the paper. At smaller scales, the distributions of simulated ice velocity fluctuations compare relatively well with buoys observations. The correlation timescale of velocity fluctuations is abnormally large in the model, suggesting incorrect spatial and/or temporal correlations of the velocity fluctuating field. Major differences between model and observations appear when analyzing the strain rates. The distributions of RGPS derived strain rates differ from the simulated distributions on a wide range of scales. The speed bias in the simulations affects the strain rates but only in terms of absolute values. This could explain the bias in the mean strain rate seen in simulations but it does not have any effect on the shape of strain rates distributions, nor on the scale dependence of strain rates.

[75] To exclude the influence of the model resolution on the discrepancy with the observations, the comparisons of strain rate distributions were done at different scales. The difference in the nature of the PDFs remains at large scale (100 km), with a clear power law decay in the observations, which does not appear in the simulated distributions. Therefore the model resolution cannot be the main cause of this problem. The fact that the shape of distributions differs suggests that the model does not represent correctly the physical processes of ice deformation.

[76] Sea ice dynamics is mainly driven by wind-forcing, which is derived from reanalysis in the simulations. Thus boundary layer turbulence and small scale variability of the wind stress on sea ice is not represented. This could partly account for the lack of large deformation rates and the smoothness of deformation fields. In other words, the part of the stochastic component of sea ice velocity which is directly linked to the short-term wind fluctuations is not represented.

[77] However, ice velocity fluctuations do not only result from short term wind-forcing. They also emanate from the ice mechanical behavior, through the internal ice stress term of the equation of motion, which is calculated by the rheology. Rampal et al. (submitted manuscript, 2009) recently detailed the importance of the ice rheology on the velocity statistics. *Weiss* [2008] showed that the intermittency of ice stresses is not inherited from wind-forcing but emerges from sea ice mechanics. This suggests that if the ice mechanics is well represented in the model, its finger-

print should appear in the ice velocity and strain rate statistics, even if the forcing is not perfect.

[78] Another consequence of the ice mechanical properties is the spatial and temporal scaling laws of sea ice deformation (relations (5) and (6)). These relations express the strong intermittency and high heterogeneity of the deformation fields [*Marsan et al.*, 2004; *Rampal et al.*, 2008] and associated space and time correlations.

[79] Since we have shown that the scaling laws are not reproduced in any of the models, and that strain rate distributions differ in shape from the observations, we argue that a possible reason for the incorrect representation of the statistical properties of sea ice deformation could be mainly due to the model physics, and more specifically the mechanical framework used in the models.

6.2. A Different Mechanical Framework for Sea Ice Mechanics?

[80] In the classical VP framework [*Hibler*, 1979], the parameterization of the ice strength P depends on the ice concentration A, inducing a weakening mechanism: a decrease in A leads to a reduced ice strength and increased deformation. The goal of this parameterization is to localize the deformation, through a positive feedback loop. However, the effects of this parameterization are limited to single grid cells, as stresses are not redistributed on the other nodes of the mesh, since the VP rheology does not consider elastic interactions. The parameterization of P appears inadequate to simulate correctly the properties of the deformation fields. The tuning of different rheology parameters, such as the creep limit in our case, proved to have insignificant effects on the results. Moreover, in such a scheme, there is no direct link between deformation (and particularly divergence), and ice concentration. This analysis commensurates with the conclusions of *Coon et al.* [2007] who suggested a different view of the dynamics of pack ice and underlined the need to directly account for velocity discontinuities in order to get a good representation of deformation.

[81] *Weiss et al.* [2007] argued that the deformation of the sea ice cover is essentially elasto-brittle, the inelastic deformation being accommodated by differential displacements along fracture and fault planes, from the scale of the ice thickness ($\sim$m) to geophysical scales (10^3 km for the Arctic basin). Considering the sea ice cover as an elastic plate, long range elastic interactions take place between fractures. Consequently, a small perturbation can trigger much larger events, and scaling laws as well as intermittency emerge naturally.

[82] It is worth noting that, using a discontinuous Lagrangian approach to explicitly model ice floes and the interactions between them such as fracturing and the propagation of stress relaxation, *Hopkins and Thorndike* [2006] reproduced the power law distribution of floe sizes in a regional model, as observed from satellite images [*Weiss and Marsan*, 2004].

[83] Following these arguments, we believe that a different mechanical framework should be developed for sea-ice in global models, introducing the long-range elastic interactions that are at the root of the scaling properties described above. Elasto-brittle models introducing a progressive damage law with an associated failure criterion

already proved to successfully reproduce the complexity and scaling properties of strain fields in the Earth's crust [*Cowie et al.*, 1995], or of rocks damage [*Amitrano et al.*, 1999].

[84] The inadequate representation of the fluctuating part of sea ice kinematics may have strong consequences in terms of ocean-atmosphere thermodynamic fluxes. These fluxes are extremely sensible to fluctuations of the open water concentration, i.e. on lead/fracture opening and closing which are themselves linked to kinematical variables (e.g., divergence). As an example, a change in the ice concentration of 1% within 48 hours induces a difference in the temperature of the atmospheric boundary layer up to 3.5 K [*Lüpkes et al.*, 2008]. Erroneous sea ice concentrations in models have a strong impact on simulations as ice concentration is one of the most important factor of the surface energy budget [*Maykut and Untersteiner*, 1971; *Sorteberg et al.*, 2007]. Furthermore, the spatial repartition of leads and polynyas also control the heat budget, since narrow leads transfer heat more efficiently than larger ones [*Andreas and Cash*, 1999]: the relationship between lead opening and heat transfer is strongly nonlinear. Consequently, average values such as average ice concentration or average strain rates contain little information to correctly simulate thermodynamic transfers.

[85] All these results demonstrate the need of a precise representation of the spatial distribution of open water and leads in numerical models. We believe that this can only be achieved if the strain rate fields are well captured. By this, we mean that statistical and scaling properties should be well represented, as the small scale stochastic component of kinematics is by nature impossible to *predict* in a deterministic sense.

7. Conclusions

[86] In this paper, ice motion from three different simulations is evaluated on the basis of statistical and scaling properties of sea ice drift and deformation. Two simulations were obtained with the Louvain-la-Neuve Ice Model (LIM) coupled to a high-resolution ocean model (12 km grid scale), one with VP ice dynamics and the other one with EVP dynamics. The third simulation was obtained with the Los Alamos Sea Ice Model (CICE), coupled to a simple ocean mixed layer (9 km grid scale).

[87] The results presented in this paper focus mainly on the two LIM simulations, which are examined in terms of mean velocity field, distributions of ice velocity fluctuations, strain rate distributions and scale dependence of strain rates. Only a few important results regarding the statistical properties of ice deformation are presented for the CICE simulation.

[88] The main conclusions of this work are:

[89] 1. At large scales (400 km, 3 months), the mean velocity field simulated by LIM is fairly well represented, although a significant bias on the simulated ice speed is noted. At finer scales, below a few hundred km and few months, the velocity field is dominated by the stochastic component of ice velocity and direct comparisons through correlation coefficients are inappropriate. Instead, simulated velocities are evaluated at small scales through the distributions of velocity fluctuations. Model and buoy distributions of velocity fluctuations compare favorably.

[90] 2. There is a strong discrepancy between model and RGPS distributions of strain rates: strain rates derived from RGPS observations exhibit "wild randomness", with power law tailed distributions, whereas simulated distributions show "mild randomness" and remain in the Gaussian attraction basin. This discrepancy persists at scales much larger than the model grid size (100 km).

[91] 3. The analysis of strain rate distributions also provided valuable information for further evaluations: the properties of RGPS distributions imply that means and standard deviations of strain rates are volatile, their value is controlled by a few extreme strain rate values. Evaluation of model strain rates should therefore consider the entire distributions and not only the means and standard deviations.

[92] 4. The models are unable to reproduce the spatial and temporal correlations of the deformation fields: In the observations, ice deformation depends of scales following specific spatial and temporal scaling laws that express the heterogeneity and the intermittency of deformation. These relations do not appear in simulated ice deformation. Mean deformation in models is almost scale independent.

[93] 5. The incorrect representation of the statistical properties of ice deformation could be mainly explained by the mechanical framework used in models: the scaling laws of deformation and the shape of strain rate distributions are properties that emanate from the ice mechanical behavior. The fact that these properties are not represented in models suggests that the modeling framework is inappropriate. A different modeling framework, including elastic interactions, could improve the representation of ice deformation in models.

References

Amitrano, D., J. Grasso, and D. Hantz (1999), From diffuse to localised damage through elastic interaction, *Geophys. Res. Lett.*, *26*, 2109–2112.

Andreas, E., and B. Cash (1999), Convective heat transfer over wintertime leads and polynyas, *J. Geophys. Res.*, *104*, 25,721–25,734.

Barnier, B., et al. (2006), Impact of partial steps and momentum advection schemes in a global ocean circulation model at eddy permitting resolution, *Ocean Dyn.*, *56*, 543–567.

Bouillon, S., M. A. M. Maqueda, V. Legat, and T. Fichefet (2009), An elastic-viscous-plastic sea ice model formulated on Arakawa B and C grids, *Ocean Model.*, *27*(3–4), 174–184.

Coon, M., R. Kwok, G. Levy, M. Pruis, H. Schreyer, and D. Sulsky (2007), Arctic Ice Dynamics Joint Experiment (AIDJEX) assumptions revisited and found inadequate, *J. Geophys. Res.*, *112*, C11S90, doi:10.1029/2005JC003393.

Cowie, P., D. Sornette, and C. Vanneste (1995), Multifractal scaling properties of a growing fault population, *Geophys. J. Int.*, *122*, 457–469.

Drakkar-Group (2007), Eddy-permitting ocean circulation hindcasts of past decades, *CLIVAR Exchanges*, *12*(3), 8–10.

Fichefet, T., and M. A. Morales-Maqueda (1997), Sensitivity of a global sea ice model to the treatment of ice thermodynamics and dynamics, *J. Geophys. Res.*, *102*, 12,609–12,646.

Fily, M., and D. Rothrock (1990), Opening and closing of sea ice leads: Digital measurements from synthetic aperture radar, *J. Geophys. Res.*, *95*, 789–796.

Frisch, U. (1995), *Turbulence: The Legacy of A. N. Kolmogorov*, Cambridge Univ. Press, Cambridge, U. K.

Heil, P., and W. Hibler (2002), Modeling the high-frequency component of arctic sea-ice drift and deformation, *J. Phys. Oceanogr.*, *32*, 3039–3057.

Hibler, W. (1979), A dynamic thermodynamics sea ice model, *J. Phys. Oceanogr.*, *9*, 815–846.

Hopkins, M. A., and A. S. Thorndike (2006), Floe formation in arctic sea ice, *J. Geophys. Res.*, *111*, C11S23, doi:10.1029/2005JC003352.

Hunke, E., and J. Dukowicz (1997), An elastic-viscous-plastic model for sea ice dynamics, *J. Phys. Oceanogr.*, *27*, 1849–1867.

Hunke, E., and W. Lipscomb (2001), CICE: The Los Alamos sea ice model, documentation and software user's manual, *Tech. Rep. LACC-98-16 v.3*, T-3 Fluid Dynamics Group, Los Alamos National Laboratory, Los Alamos, N. M. (Available at http://climate.lanl.gov/models/cice/)

Kwok, R. (1998a), Sea ice motion from satellite passive microwave imagery assessed with ERS SAR and buoy motions, *J. Geophys. Res.*, *103*, 8191–8214.

Kwok, R. (1998b), The RADARSAT geophysical processor system, in *Analysis of SAR Data of the Polar Oceans: Recent Advances*, edited by C. Tsatsoulis and R. Kwok, chap. 11, pp. 235–257, Springer, London, U. K.

Kwok, R. (2001), Deformation of the Arctic Ocean sea ice cover between November 1996 and April 1997: A survey, in *Scaling Laws in Ice Mechanics and Ice Dynamics*, pp. 315–322, Kluwer Acad., Dordrecht, Netherlands.

Kwok, R., E. C. Hunke, W. Maslowski, D. Menemenlis, and J. Zhang (2008), Variability of sea ice simulations assessed with RGPS kinematics, *J. Geophys. Res.*, *113*, C11012, doi:10.1029/2008JC004783.

Lindsay, R., and H. Stern (2003), The RADARSAT geophysical processor system: Quality of sea ice trajectory and deformation estimates, *J. Atmos. Oceanic Technol.*, *20*, 1333–1347.

Lindsay, R., J. Zhang, and D. Rothrock (2003), Sea-ice deformation rates from satellite measurements and in a model, *Atmos. Ocean*, *41*, 35–47.

Lipscomb, W. (2001), Remapping the thickness distribution in sea ice models, *J. Geophys. Res.*, *106*, 13,989–14,000.

Lüpkes, C., T. Vihma, G. Birnbaum, and U. Wacker (2008), Influence of leads in sea ice on the temperature of the atmospheric boundary layer during polar night, *Geophys. Res. Lett.*, *35*, L03805, doi:10.1029/2007GL032461.

Marsan, D., H. Stern, R. Lindsay, and J. Weiss (2004), Scale dependence and localization of the deformation of Arctic sea ice, *Phys. Rev. Lett.*, *17*, doi:10.1103/PhysRevLett.93.178501.

Martin, S., and A. Thorndike (1985), Dispersion of sea ice in the Bering sea, *J. Geophys. Res.*, *90*, 7223–7226.

Maslowski, W., and W. Lipscomb (2003), High resolution simulations of Arctic sea ice, 1979–1993, *Polar Res.*, *22*, 67–74.

Maykut, G. (1982), Large scale heat exchange and ice production in the central Arctic, *J. Geophys. Res.*, *87*, 7971–7984.

Maykut, G., and N. Untersteiner (1971), Some results from a time dependent thermo-dynamic model of sea ice, *J. Geophys. Res.*, *76*, 1550–1575.

Moritz, R., and H. Stern (2001), Relationships between geostrophic winds, ice strain rates and the piecewise rigid motions of pack ice, in *Scaling Laws in Ice Mechanics and Ice Dynamics*, edited by J. P. Dempsey and H. H. Shen, pp. 335–348, Kluwer Acad., Dordrecht, Netherlands.

Moritz, R., C. Bitz, and E. Steig (2002), Dynamics of recent climate change in the Arctic, *Science*, *297*, 1497–1502.

Nye, J. F. (1973), Is there any physical basis for assuming linear viscous behavior for sea ice?, *AIDJEX Bull.*, *21*, 18–19.

Rampal, P., J. Weiss, D. Marsan, R. Lindsay, and H. Stern (2008), Scaling properties of sea ice deformation from buoy dispersion analyses, *J. Geophys. Res.*, *113*, C03002, doi:10.1029/2007JC004143.

Rampal, P., J. Weiss, and D. Marsan (2009), Positive trend in the mean speed and deformation rate of Arctic sea ice, 1979–2007, *J. Geophys. Res.*, *114*, C05013, doi:10.1029/2008JC005066.

Rothrock, D. (1975), Energetics of plastic-deformation of pack ice by ridging, *J. Geophys. Res.*, *80*, 4514–4519.

Sornette, D. (2000), *Critical Phenomena in Natural Sciences*, Springer, Berlin.

Sorteberg, A., V. Kattsov, J. T. Walsh, and A. F. Pavlova (2007), The Arctic surface energy budget as simulated with the IPCC AR4 AOGCMs, *Clim. Dyn.*, *29*, 131–156.

Taylor, P., D. Feltham, P. Sammonds, and D. Hatton (2006), Continuum sea ice rheology determined from subcontinuum mechanics, *J. Geophys. Res.*, *111*, C11015, doi:10.1029/2005JC002996.

Thomas, D. (1999), The quality of sea ice velocity estimates, *J. Geophys. Res.*, *104*, 13,627–13,652.

Thorndike, A. (1986), Kinematics of sea ice, in *The Geophysics of Sea Ice*, pp. 489–549, Plenum, New York.

Thorndike, A. S., and R. Colony (1980), Arctic ocean buoy program data report, 19 January 1979–31 December 1979, technical report, Applied Physics Laboratory, Univ. of Washington, Seattle, Wash.

Thorndike, A., and R. Colony (1982), Sea ice motion in response to geostrophic winds, *J. Geophys. Res.*, *87*, 5845–5852.

Weiss, J. (2008), Intermittency of principal stress directions within Arctic sea ice, *Phys. Rev. E*, *77*, doi:10.1103/PhysRevE.77.056106.

Weiss, J., and D. Marsan (2004), Scale properties of sea ice deformation fracturing, *C. R. Phys.*, *5*, 735–751.

Weiss, J., E. Schulson, and H. Stern (2007), Sea ice rheology from in-situ, satellite and laboratory observations: Fracture and friction, *Earth Planet. Sci. Lett.*, *255*(1–2), 1–8, doi:10.1016/j.epsl.2006.11.033.

Weiss, J., D. Marsan, and P. Rampal (2009), Space and time scaling laws induced by the multiscale fracturing of the arctic sea ice cover, in *IUTAM Symposium on Scaling in Solid Mechanics*, edited by F. M. Borodich, pp. 101–109, Springer, New York.

Zhang, J., D. Rothrock, and M. Steele (2000), Recent changes in arctic sea ice: The interplay between ice dynamics and thermodynamics, *J. Clim.*, *13*, 3099–3114.

Zhang, H. M., M. Prater, and T. Rossby (2001), Isopycnal lagrangian statistics from the north atlantic current rafos float observations, *J. Geophys. Res.*, *106*, 13,817–13,836.

————————————

B. Barnier and J. M. Molines, Laboratoire des Ecoulements Géophysiques et Industriels, MEOM, BP 53, F-38041 Grenoble Cedex 9, France.

S. Bouillon, G. Lemaître Institute of Astronomy and Geophysics (ASTR), Université Catholique de Louvain, 2 Chemin du Cyclotron, B-1348 Louvain-la-Neuve, Belgium.

L. Girard and J. Weiss, Laboratoire de Glaciologie et Geophysique de l'Environnement, CNRS-UJF Grenoble, 54 rue Molière, BP 96, F-38400 St. Martin d'Hères Cedex, France. (lgirard@lgge.obs.ujf-grenoble.fr)